Preparation of GO/MIL-101(Fe,Cu) composite and its adsorption mechanisms for phosphate in aqueous solution

You Wu (securewyy@126.com)
College of Geology and Environment, Xi'an University of science and technology
Zuannian Liu
College of geology and environment, Xi'an University of Science and Technology
Bakhtari Mohammad Fahim
College of Geology and Environment, Xi'an University of Science and Technology
Junnan Luo
College of Geology and Environment, Xi'an University of Science and Technology

Research Article

Keywords: MOFs, phosphate, GO, composite, adsorption, wastewater treatment

Posted Date: February 19th, 2021

DOI: https://doi.org/10.21203/rs.3.rs-191207/v1

Preparation of GO/MIL-101(Fe,Cu) composite and its adsorption mechanisms for phosphate in aqueous solution

You Wu[1]; Zuannian Liu[1]; Bakhtari Mohammad Fahim[1]; Junnan Luo[1]

College of Geology and Environment, Xi'an University of science and technology, Xi'an, 710054, PR China

Corresponding author: You Wu (securewyy@126.com)

Abstract: In this study, MIL-101(Fe), MIL-101(Fe,Cu), and Graphene Oxide (GO) /MIL-101(Fe,Cu) were synthesized to compose a novel sorbent. The adsorption properties of these three MOFs-based composites were compared toward the removal of phosphate. Furthermore, the influencing factors including reaction time, pH, temperature and initial concentration on the adsorption capacity of phosphate on these materials as well as the reusability of the material were discussed. The structure of fabricated materials and the removal mechanism of phosphate on the composite material were analyzed by Scanning electron microscopy (SEM), Fourier transform infrared spectroscopy (FTIR), X-ray diffraction (XRD), X-ray photoelectron spectroscopy (XPS), nitrogen adsorption-desorption analysis and zeta potential. The results show that the maximum adsorption capacity of phosphate by the composite GO/MIL-101(Fe,Cu)-2% was 204.60 $mg \cdot g^{-1}$, which is higher than that of MIL-101(Fe,Cu) and MIL-101(Fe). likewise the specific surface area of GO/MIL-101(Fe,Cu)-2% is 778.11 m^2/g is higher than that of MIL-101(Fe,Cu) and MIL-101(Fe),which are 747.75 and 510.66m^2/g respectively. The adsorption mechanism of phosphate is electrostatic attraction, form coordination bonds and hydrogen bonds. The fabricated material is a promising adsorbent for the removal of phosphate with good reusability.

Keywords: MOFs; phosphate; GO; composite; adsorption; wastewater treatment

INTRODUCTION

Water pollution has gradually become a serious global issues (Santana et al. 2020; Strokal et al. 2020; Deletic et al. 2019), due to rapid urbanization , industrialization, agriculture activities over past decades which caused in contamination of water bodies. Many industries discharge their sewage/waste into water bodies without pre-treatment which contains several traditional chemicals such as heavy metal ions, hazardous and toxic pollutants. Among different water contaminates, one is excessive growth of alages (especially Cyanobacterai) which associated with accumulation of phosphors in water, result in eutrophication phenomenon (Sarma et al. 2020; Huang et al.

2017). Consequently, the aquatic organisms in water will be reduced due to eutrophication phenomenon, and eventually lead to the gradual extinction of the entire regional water ecosystem (Liu et al. 2018). Studies have shown that phosphate is sufficient to stimulate the growth of algae when it is as low as 0.02mg/L (Bacelo et al. 2020; Isiuku et al. 2020; Ogata et al. 2020; Al-Alwani et al. 2018). At present, numerous technologies have been applied for the treatment of phosphate, such as biological method (Buhmann et al. 2013), flocculation (Langer et al. 2017) membrane filtration (Leo et al. 2011) and adsorption (Drenkova-Tuhtan et al. 2017; Loganathan et al. 2014), etc. Among them, adsorption has received extensive attention due to its high removal efficiency, wide removal range, simple operation and eco-friendly (Adegoke et al. 2015; Crini et al. 2006; Srinivasan et al. 2010).

Metal organic framework (MOFs) is a new type of organic synthetic adsorption material. As an organic-inorganic hybrid metal organic framework containing organic ligands and metal clusters, it has not only ultra-high surface area and pore volume, but also an adjustable surface area, and excellent physio-chemical properties (i.e. unsaturated metal sites, pore size and geometry) (Rego et al. 2021; Emam et al. 2020). Its composite materials are often used in the adsorption of pollutants in water (Liu et al. 2020; Liu et al. 2020). Compared with single-metal MOFs materials, bi-metal MOFs materials have two metal active sites and can significantly improve the specific surface area, capacitance and other properties of the material (Hou et al. 2019; Liu et al. 2020), which result in wide application and extensively studies of them. Many research has been done and proved the excellent adsorption performance of it toward the removal of water pollutants (Gu et al. 2019; El-Yazeed et al. 2020).

Carbon materials are one of the most widely used adsorption materials, and graphene oxide is one of the most excellent materials (Nebol'sin et al. 2020; Tian et al. 2021), since it has large specific surface area, mechanical flexibility, thermal stability and plenty of oxygen-containing functional groups present on its surface (Kyzas et al. 2018; Burakov et al. 2018). Furthermore, its monomer material has good adsorption performance (Lai et al. 2018; Lebron et al. 2020), and some researchers have made it into a membrane structure to adsorb pollutants (Li et al. 2020). However, graphene oxide is often difficult to remove in water due to its dispersibility and hydrophilicity properties. Therefore, many researchers attempted to overcome such defect by combining GO with other materials. (Zhang et al. 2020; Chen et al. 2020). Many studies have

been done by researchers and found that coating the surface with other materials (such as MOF) is considered to be a good way to avoid its defects, and GO-MOF composite material is hence considered to be a good composite adsorption material (Zhou et al. 2014; Amini et al. 2020; Eltaweil et al. 2020; Bu et al. 2019).

We expect to prepare a bimetallic MOF of Fe and Cu and combine it with GO to form a coating structure with a large layer of small crystals through self-assembly in the reactor, and synthesize a new type of composite adsorption material. In this study we fabricated MIL-101(Fe), MIL-101(Fe,Cu) and GO/MIL-101(Fe,Cu) by hydrothermal method. The crystalline morphology of MIL-101(Fe,Cu) has been changed by adding of Cu, and the specific surface area was significantly increased. Moreover, After the addition of GO, MIL-101(Fe,Cu) grew on the surface GO, which contained a large number of oxygen-containing functional groups, result in formation of a tight coating structure. Finally, a new type of composite adsorption material obtained. The optimal ratio of the two was determined by adjusting the addition amount of GO and MIL-101(Fe,Cu).

2. Materials and methods

2.1 Experimental materials

Chemical substances used in the preparation, including iron chloride hexahydrate ($FeCl_3 \cdot 6H_2O$), copper nitrate trihydrate ($Cu(NO_3)_2 \cdot 3H_2O$), terephthalic acid ($C_8H_6O_4$), N,N-dimethylformamide (DMF) (C_3H_7NO), which were purchased from Sinopharm Chemical Reagent Co., Ltd. Other chemicals, absolute ethanol, potassium dihydrogen phosphate (KH_2PO_4), potassium antimony tartrate ($C_8H_4K_2O_{12}Sb_2$), ascorbic acid ($C_6H_8O_6$) were all of analytically pure, and they were supplied by Sinopharm Chemical Reagent Co., Ltd. The deionized water was used for experiment. The deionized (DI) water was used for preparing the solution and washing the prepared samples.

2.2 Preparation of MIL-101 (Fe), MIL-101 (Fe, Cu), GO/MIL-101 (Fe, Cu) composite adsorption materials

(1) MIL-101(Fe): 0.831g terephthalic acid and 1.461g ferric chloride hexahydrate were added to 30ml DMF, and then stirred at room temperature for 1h. The obtained mixture was kept in a 100ml autoclave lined with Teflon liner at 120°C for 24h. Subsequently, it was washed with DMF and absolute ethanol three times and dried in an oven at 60°C till its mass remained unchanged.

(2) MIL-101(Fe,Cu): It was prepared in the same way as MIL-101(Fe), except the addition of 0.302g copper nitrate trihydrate into 0.831g of terephthalic acid and 1.461g of ferric chloride hexahydrate.

(3) GO/MIL-101(Fe,Cu): 0.831g terephthalic acid, 1.461g ferric chloride hexahydrate and 0.302 copper nitrate trihydrate were dissolved in 30ml DMF and stirred continuously at room temperature for 1h. An appropriate amount of GO was added to 6ml ethanol, which was dispersed by ultrasound and then added to the above solution. The ultrasonic wave lasted 20 min. The obtained mixture was kept in a 100ml autoclave lined with Teflon liner at 120°C for 24h. Subsequently, it was washed with DMF and absolute ethanol three times and dried in an oven at 60°C till its mass remained unchanged. GO is added in the composite material at a weight ratio of 1%, 2%, 5%, 10%, 20%.

2.3 Characterization of the adsorbent

The FE-SEM S4800 (produced by Hitachi, Japan) electron microscope was used to scan the adsorbent material to observe its surface structure and microscopic composition. The XD-3 type X-ray powder diffraction was used for the test, and the measurement conditions were: the copper target Kα rays,the scanning step is 0.02°, and the scanning range 2θ is 5~75°. The Fourier transform infrared absorption spectrum was detected by Nicolet iS50 FTIR spectrometer (Thermo Fisher, USA). JW-BK122W N_2 physical adsorption device (produced by Beijing Jingwei Gaobo Science and Technology Co., Ltd.) was used to test the adsorbent material. X-ray photoelectron spectroscopy analysis was conducted by ESCALAB250Xi (Thermo Fisher, USA) photoelectron spectrometer under AlKα radiation. The zeta potential of the sample was measured by the JS94H microelectrophoresis instrument.

2.4 Experiment on adsorption performance

To study the adsorption performance of the prepared material a 100mg·L^{-1} sample solution was prepared and placed in a 1000ml volumetric flask. Then 100ml of the sample take out place in an Erlenmeyer flask for further usage. To investigate the effect of prepared material different concentration of the solution with various dosage of the adsorbent were used under the condition of influencing parameters. The absorbance was measured by UV-vis spectrophotometer and the concentration was calculated. The pH, temperature and dosage of the experiment were adjusted respectively to explore the effect of different influencing parameters on the adsorption process.

The removal rate and adsorption capacity were calculated by the following formulas:

$$q_e = \frac{(C_0 - C_e)V}{m} \quad (1)$$

$$\eta = \frac{(C_0 - C_t)}{C_0} \times 100\% \quad (2)$$

where q_e is adsorption capacity at adsorption equilibrium, $mg \cdot g^{-1}$; C_0 is initial concentration of simulated wastewater, $mg \cdot L^{-1}$; C_e is concentration of simulated wastewater at adsorption equilibrium, $mg \cdot L^{-1}$; V is volume of simulated wastewater, L; m is the mass of the adsorbent; η is removal efficiency, %; C_0 is initial mass concentration of phosphate solution, $mg \cdot L^{-1}$; C_t is the mass concentration of phosphate after degradation, $mg \cdot L^{-1}$.

3. Results and discussion

3.1 Surface morphology

The SEM image of MIL-101(Fe) is shown in Figure 1(a). as it can be seen MIL-101(Fe) shows a uniform and smooth octahedral structure with clear and orderly edges and corners, which is in line with previous reported research (Barbosa et al. 2017). Compared with MIL-101(Fe), the edges and corners of the MIL-101(Fe,Cu) crystals had less obvious edges and angles, which were not as regular as the previous ones, and the surface morphology became rough. This might be due to the addition of Cu for replacing some Fe sites, the radius of Cu^{2+} is larger than that of Fe^{3+}, result in a larger specific surface area. As shown in Figure 1(d)-(e), after 2% GO was added, the crystal morphology of MIL-101(Fe,Cu) did not change, and it could still be successfully synthesized and attached to the surface of GO. Many MIL-101(Fe,Cu) crystals covered most of the GO surface, forming a new type of composite material with a large number of small crystals wrapped in large layers, formed a tight structure. Figure 1(f) indicate that when 10% GO was added, the crystal shape become more distorted, and some spheres are attached to the GO surface. This might be due to a large amount of GO inadvertently hindering the synthesis of MIL-101(Fe,Cu) crystals.

3.2 Crystal structure

The main diffraction peaks of MIL-101(Fe) appeared at 2θ=8.99, 9.23, 18.88, 23.16°, which is according to the results of previous studies (Lin et al. 2020), which was proven that MIL-101(Fe) was successfully synthesized. The position of the main diffraction peak of MIL-101(Fe,Cu) was basically the same as that of MIL-101(Fe), and the position of the peak was slightly shifted to the

left because the radius of the doped Cu particles is larger than that of Fe, thus result in slight lattice distortion. It is precisely because of such distortion that the specific surface area of MIL-101(Fe,Cu) was significantly improved. The XRD results did not remarkably change after adding a small amount of GO, since GO was a single-layer sheet structure that had been ultrasonically processed and its dosage was small. No peak could be observed in the XRD image. However, as the amount of GO doped increased, the position of the diffraction peak greatly changed. GO sheet layer blocked the binding and reaction of the precursor materials, so the peak of the precursor substance rather than that of MIL-101(Fe,Cu) was observed in the XRD image captured at this point, which is also consistent with the SEM results.

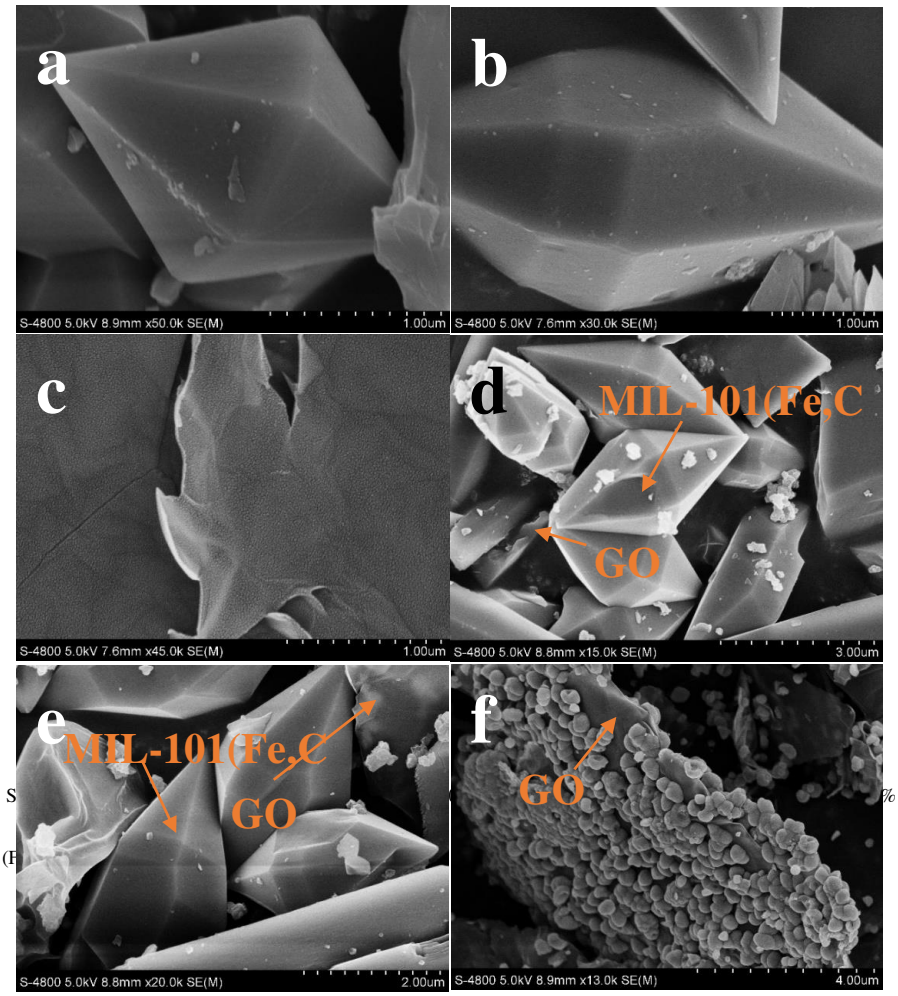

Figure 1. S % (d-e) and GO/MIL-101(F

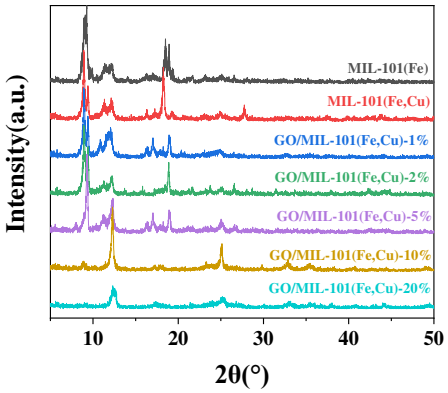

Figure 2. XRD patterns of samples.

3.3 N_2 adsorption-desorption analysis

As it can be seen from Table 1, after Cu was added, the specific surface area of MIL-101(Fe) significantly increased from 510.66 $m^2 \cdot g^{-1}$ to 747.75 $m^2 \cdot g^{-1}$. The surface of the material was exposed to more active sites, which was conducive to the adsorption process. After GO was added, the specific surface area of the sample slightly increased.

It can be seen from the adsorption-desorption curve that the adsorption capacity of MIL-101(Fe) and MIL-101(Fe,Cu) rose rapidly at a lower relative pressure, and the adsorption saturation value appeared after reaching a certain relative pressure. The results are consistent with those indicated in (Li et al. 2019). The adsorption-desorption curve has the characteristics of a typical Type-I isotherm. This proves that the sample contains micropores or mesopores which are very close to the micropore size.

What I want to express in this sentence is that the pores in the material are micropores or mesopores that are very close to the size of the micropores. However, GO/MIL-101(Fe,Cu)-2% had the characteristics of both Type-I and Type-II isotherms, and the hysteresis ring conforms the characteristics of the H4 type hysteresis ring, which often appears on the mixed pore size adsorbent with both micropores and mesoporous (Dollimore et al. 1976).

Table 1. Specific surface area and pore structure parameter of sample.

Samples	S_{BET}($m^2 \cdot g^{-1}$)	*Vp* ($cm^3 \cdot g^{-1}$)	d_P(nm)
MIL-101(Fe)	510.66	0.36	2.75
MIL-101(Fe,Cu)	747.75	0.49	2.63
GO/MIL-101(Fe,Cu)	778.11	0.55	2.57

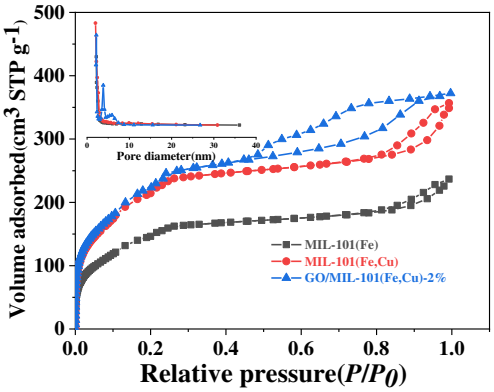

Figure 3. N_2 adsorption–desorption isotherms and corresponding pore size distribution curves(inset) of samples.

3.4 FTIR spectrum

As shown in Figure 4, the characteristic peaks of MIL-101(Fe) appeared at 543.92, 748.71, 1389.60, 1507.25, 1541.24, 1669.00 and 3324.25 cm^{-1}, respectively. The peak at 3324.25 cm^{-1} came from -OH in water molecules. The absorption peaks at 1669.00, 1541.24 and 1389.60 cm^{-1} corresponded to the symmetric and asymmetric stretching vibrations of the organic ligand O-C=O. The small absorption peak at 1507.25 cm^{-1} came from the C=C bond of the benzene ring vibration. The absorption peak at 543.92 and 748.71 cm^{-1} came from the chelating bond formed by Fe^{3+} and carboxylic acid functional group, which is consistent with the results of previous studies (Fakhri et al. 2020). The characteristic peaks of MIL-101(Fe,Cu) were basically the same as those of MIL-101(Fe). Only the peak at 1554.03 cm^{-1} was slightly blue-shifted, which was possibly caused by the carboxyl group in terephthalic acid and Cu^{2+}. As a metal active site binding with organic ligands, it had a certain impact on the iron base, causing two metal ions to compete with each other to cooperate with terephthalic acid. After GO was added, the absorption peaks of the composite material at 1541.24 and 1669.00 cm^{-1} were significantly weakened because the GO surface contained a large number of oxygen-containing functional groups that reacted with the carboxyl groups on MIL-101(Fe,Cu), and finally, a series of irregular C=O chains are generated while the number of free carbonyl C=O bonds decreases. These indicate that GO was successfully incorporated into and interacted with MIL-101(Fe,Cu). After the composite material adsorbed phosphate, two new characteristic peaks appeared at 1018.29 and 1106.69 cm^{-1}, which indicated that P=O and P-OH were formed and that the M-OH group in the composite material might be coordinated by M-O-P. The M-OH group in the composite material may adsorb phosphate through

the M-O-P coordination bond. The results indicate that the phosphate was successfully adsorbed on the composite material. After the adsorption of phosphate, the peak intensity of the composite material at 3300 cm^{-1} increased slightly. This result indicates that a hydrogen bond (O-H···O) may be formed between the phosphate and the composite material.

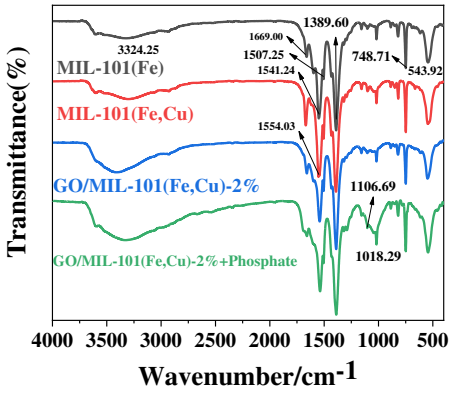

Figure 4. FTIR spectra of samples and GO/MIL-101(Fe,Cu)-2% after adsorption of phosphate.

3.5 XPS spectrum

The XPS spectrum is shown in Figure 5, and the surface atomic content is shown in Table 2. Figure 5(a) shows that the spectra of MIL-101(Fe), MIL-101(Fe,Cu), GO/MIL-101(Fe,Cu) -2%, which implies that O, C, and Fe all existed in the three samples. Cu existed in MIL-101(Fe,Cu) and GO/MIL-101(Fe,Cu)-2%, but due to the its small content, the peaks were not obvious. By adding GO, the relative intensity of the peak at C 1s was increased. Figure 5(b) shows the high-resolution images of the three samples in the Fe 2p region. MIL-101(Fe) has two peaks corresponding to Fe 2p3/2 and Fe 2p1/2 orbitals at 711.52 eV and 724.86 eV respectively (Wang et al. 2020; He et al. 2019). After Cu was added, the binding energy shifted slightly to the positive direction, and the content of Fe decreased slightly, however the content of Cu increased from 0 to 0.92%, which proved the successful incorporation of Cu. When GO was added, the binding energy moved forward, demonstrating the correlation between GO and MIL-101(Fe,Cu), which is a line with the results of FTIR. The image of Cu 2p is shown in Figure 5(c). There is no photoelectron peak in MIL-101(Fe), and the peaks of MIL-101(Fe,Cu) and GO/MIL-101(Fe,Cu)-2% appeared at 932.5 eV. The weak photoelectron peak proved the successful incorporation of Cu, but the peak was not obvious due to the small amount of incorporation. Figure 5(d) shows the high resolution spectra of C 1s in MIL-101(Fe), MIL-101(Fe,Cu), GO/MIL-101(Fe,Cu)-2%, and MIL-101(Fe).

There were three photoelectron peaks at 284.82, 286.18 and 288.75eV, corresponding to the C-C/C=C, C-O, and C=O bonds, respectively. The C=C bond came from the organic ligand and the benzene ring of graphene oxide, and the C-O bond came from the ligand. The carboxyl group and hydroxyl group on the surface of graphene oxide, and the C=O bond came from the organic ligand neutralizing the carboxyl group on the surface of graphene oxide. After GO was incorporated, the content of C atoms increased significantly, proving the successful incorporation of GO.

Table 2. Surface atom content of MIL-101(Fe), MIL-101(Fe, Cu) and GO/MIL-101(Fe, Cu)-2% composite materials.

Sample	Element content			
	C (%)	O (%)	Fe (%)	Cu (%)
MIL-101(Fe)	63.48	29.97	6.55	0
MIL-101(Fe,Cu)	61.38	31.19	6.51	0.92
GO/MIL-101(Fe,Cu)-2%	65.07	27.75	6.35	0.83

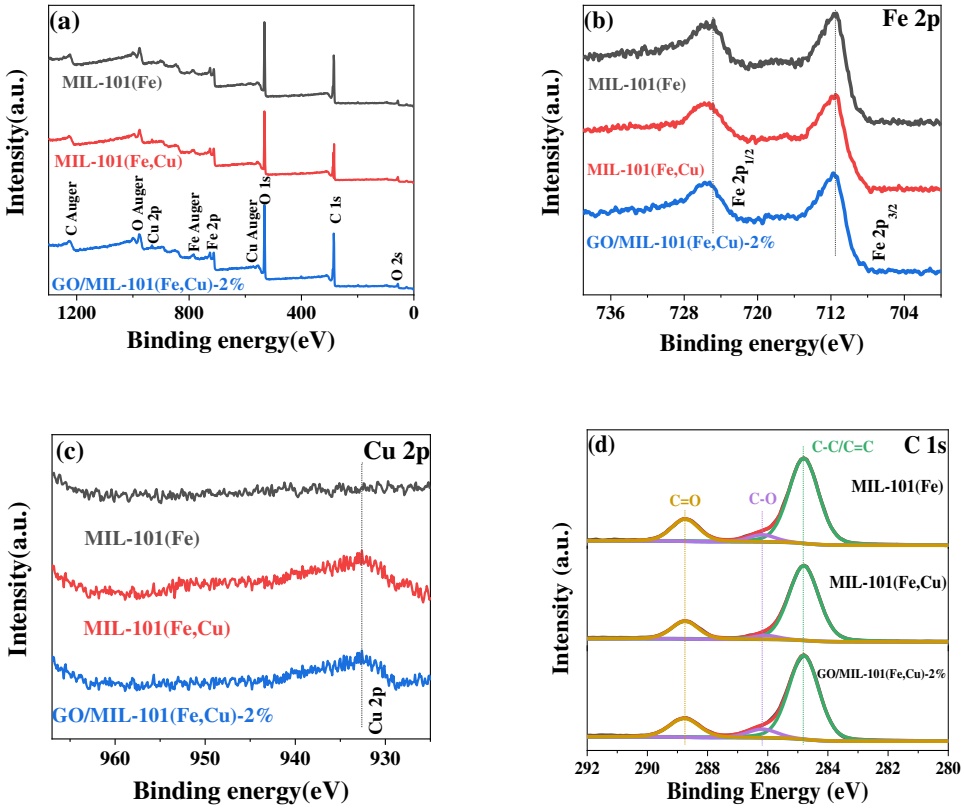

Figure 5. XPS survey spectra (a). High-resolution XPS of Fe 2p(b), Cu 2p(c), and C 1s regions(d) of samples.

3.6 Analysis of zeta potential

Figure 6 shows the zeta potential distribution curves of three samples of MIL-101(Fe), MIL-101(Fe,Cu), and GO/MIL-101(Fe,Cu)-2%, at pH=7. The zeta potentials of the materials were

10.42, 19.17, and 5.22mV, respectively, and the Isoelectric point (IEP) were all greater than 7. therefore, the three samples were positively charged under neutral conditions. It has been reported that the IEP of GO was between 3 and 4 (Zheng et al. 2019), hence a large number of oxygen-containing groups on the surface and edges tended to protonate. However, GO was negatively charged under neutral conditions. In the composite material, the surface of GO cannot completely covered by MIL-101(Fe,Cu); thus, the zeta potential of the composite material is lower than that of pure MIL-101(Fe,Cu), indicating that all three samples could absorb negative ionic pollutants through electrostatic interaction.

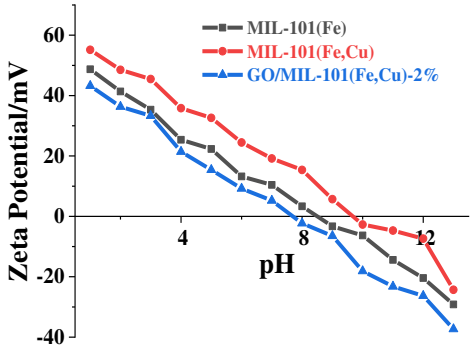

Figure 6. Distribution of zeta potentials of samples in aqueous solution.

3.7 Effect of pH

It can be seen from Figure 7 that when the pH increased from 2 to 3, the adsorption capacity increased significantly, and it decreased with the increase of pH because the phosphate existed in the form of H_3PO_4 in water when the pH was 2.13, at this point, phosphate could not be adsorbed by electrostatic effect, and the adsorption effect was poor. When the pH was greater than 2.13, the phosphate existed in the form of negative charge. Under the subsequent acidic conditions, the water contained a lot of H^+, and the surface of the adsorbent itself was positively charged. Therefore, under strong acid conditions, the adsorption capacity was significantly improved due to the presence of static electricity. As the pH rise, H^+ in water decreased, while OH^- increased which result in repulsion between adsorbent and pollutant under strong alkaline condition. Therefore, the amount of adsorption gradually decreased.

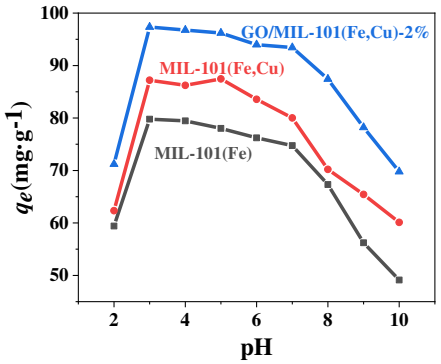

Figure 7. Effect of pH on adsorption of phosphate onto samples.

3.8 Adsorption kinetics

As it can be seen from Figure 8, the adsorption rate was great at the beginning of the reaction (before 30 min) due to presence of a large number of active sites on the sample surface result in rapid adsorption of phosphate. After 90 min as a large number of adsorption sites were filled; thus, the adsorption rate of the reaction gradually decreased and the adsorption capacity tended to saturate. The adsorption capacity of GO/MIL-101(Fe,Cu) for phosphate was superior when a small amount of GO was added. Among them, GO/MIL-101(Fe,Cu)-2% exhibited a high adsorption capacity of 204.6mg/g.

Lagergren first-order reaction kinetics was used respectively to further discuss the adsorption process. The experimental data of phosphate adsorption by three samples were fitted with the scientific model and the kinetic model of secondary reaction.

The linear form of Lagergren first-order adsorption kinetic equation is:

$$\log(q_e - q_t) = \log q_e - \frac{k_1}{2.303} t \quad (3)$$

The pseudo-second-order reaction rate equation:

$$\frac{t}{q_t} = \frac{1}{k_2 q_e^2} + \frac{1}{q_e} t \quad (4)$$

The Lagergren primary and secondary reaction rate equations were used to process the data in Figure 8. The results are shown in Figures 9 and 10, and the regression parameters are shown in Table 3.

It can be seen from Table 3 that the degree of fit between the adsorption of phosphate and the Lagergren pseudo-second-order adsorption kinetic model was higher.

Table 3. Parameters in the two kinetic models for phosphate adsorption by MIL-101(Fe), MIL-101(Fe,Cu) and GO/MIL-101(Fe,Cu)-2% composite materials.

Adsorbents	q_e mg·g^{-1}	Pseudo-first-order model			Pseudo-second-order model		
		k_1 min^{-1}	$q_{e.c}$ mg·g^{-1}	R^2	k_2 g·mg^{-1}·min^{-1}	$q_{e.c}$ mg·g^{-1}	R^2
MIL-101(Fe)	73.7406	0.02982	46.14	0.9679	0.0013	77.82	0.9981
MIL-101(Fe,Cu)	81.0108	0.02331	40.09	0.9614	0.0013	84.39	0.9993
GO/MIL-101(Fe,Cu)	95.4374	0.0322	49.014	0.9859	0.0012	96.53	0.9995

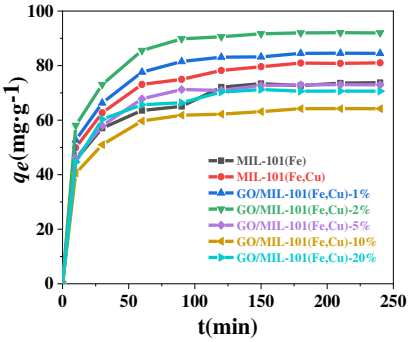

Figure 8. Adsorption of phosphate onto samples at different adsorption time.

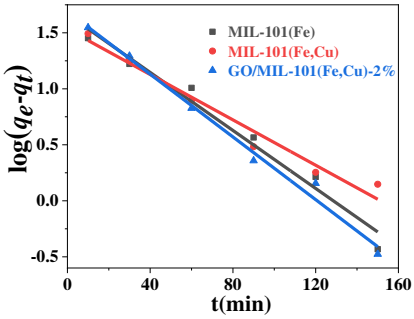

Figure 9. Lagergren first-order kinetics equation plot of phosphate.

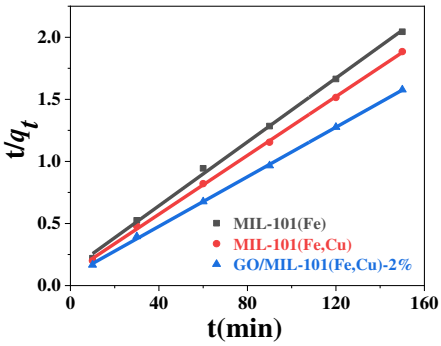

Figure 10. Lagergren second-order kinetics equation plot of phosphate.

3.9 Adsorption isotherm

It can be seen from the Figure 11 that the adsorption amount of phosphate of the three samples

increased with the increase of C_e and slightly became gentle. When C_e is low, the adsorption site of the adsorbent has a low filling rate of phosphate. With the increase of the concentration, the filling rate gradually increased and the adsorption gradually reached saturation, and the adsorption effect of GO/MIL-101(Fe,Cu) -2% was better than that of MIL-101(Fe) and MIL-101(Fe,Cu).

The Langmuir adsorption isotherm model and the Freundlich adsorption isotherm model were used to process the data in Figure 11. The results are shown in Figures 12 and 13, and the regression parameters are shown in Table 4. According to the table, the adsorption of phosphate by MIL-101(Fe), MIL-101(Fe,Cu) and GO/MIL-101(Fe,Cu)-2% was similar to that of Langmuir adsorption isotherm model, and the linear correlation coefficient R^2 was greater than the Freundlich model. That is, the adsorption process is a single layer adsorption. According to the Langmuir isotherm model, the calculated maximal adsorption quantities of the MIL-101(Fe), MIL-101(Fe,Cu) and GO/MIL-101(Fe,Cu)-2% towards phosphate are 161.24, 182.88 and 204.6 $mg \cdot g^{-1}$, respectively. The adsorption capacities of GO/MIL-101(Fe,Cu)-2% is better than that of MIL-101(Fe) and MIL-101(Fe,Cu). Futhermore, Table 5 shows that the adsorption capacities of GO/MIL-101(Fe,Cu)-2% towards phosphate are higher than or comparable than that other adsorption materials.

The Langmuir adsorption isotherm equation is:

$$\frac{1}{q_e} = \frac{1}{Q^0} + \left(\frac{1}{bQ^0}\right)\left(\frac{1}{C_e}\right) \quad (5)$$

where Q_0 is the unit saturated adsorption capacity when the monolayer is formed, $mg \cdot g^{-1}$; C_e is the equilibrium mass concentration of the solution, $mg \cdot L^{-1}$; q_e is the equilibrium adsorption capacity, $mg \cdot g^{-1}$; b is the constant of Langmuir equilibrium. The Freundlich adsorption isotherm equation is:

$$\log q_e = \log K_F + \frac{1}{n}\log C_e \quad (6)$$

where K_F and n are adsorption constants related to factors such as temperature and specific surface area of the adsorbent.

Table 4. Parameters of the Langmuir and Freundlich isotherm models for phosphate adsorption onto MIL-101(Fe), MIL-101(Fe,Cu) and GO/MIL-101(Fe,Cu)-2% composite.

Adsorbents	Langmuir			Freundlich		
	Q^0/mg·g^{-1}	b/L·mg^{-1}	R^2	K_F	n	R^2
MIL-101(Fe)	167.22	0.0205	0.9901	18.17	2.84	0.90877
MIL-101(Fe,Cu)	186.92	0.0297	0.9995	24.87	3.03	0.88912
GO/MIL-101(Fe,Cu)	208.33	0.0489	0.9994	34.54	3.32	0.88223

Table 5. Comparison of adsorption capacities of GO/MIL-101(Fe,Cu)-2% towards phosphate with other adsorbents.

samples	Phosphate concentration(mg·L^{-1})	Adsorption equilibrium time(min)	The maximum adsorption capacity(mg·g^{-1})	Reference
GO/MIL-101(Fe,Cu)	100	90	204.6	This work
Fe-La/MgO-2	40	40	38.82	Sun et al. 2020
Mesoporous ZrO_2 fibers	75,100,150	200	222.79	Dong et al. 2020
Zn–Fe LDH	2000	15	36	Gupta et al. 2020
Fe_3O_4/CS/PEI nanoparticles	25-300	180	50.8	Fu et al. 2020
ZIF8@MWCNT nanocomposite	1000	-	203.0	Wang et al. 2020
Ce-MOF-500(S)	100	120	189.4	He et al. 2020
La/Fe_3O_4-BC	500	300	20.5	Wang et al. 2019

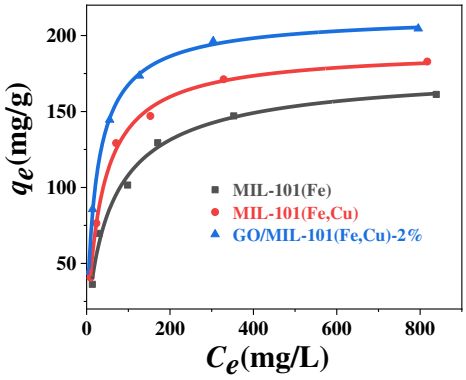

Figure 11. Phosphate adsorption isotherms for samples.

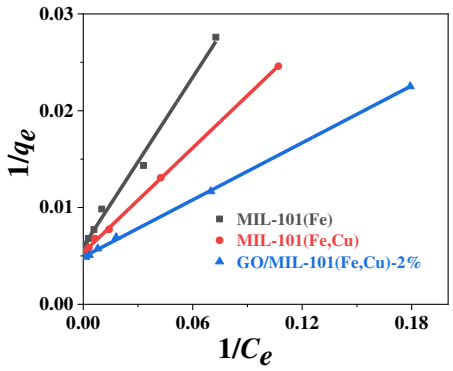

Figure 12. Fitting results of linearized Langmuir adsorption isotherms of phosphate adsorption on samples.

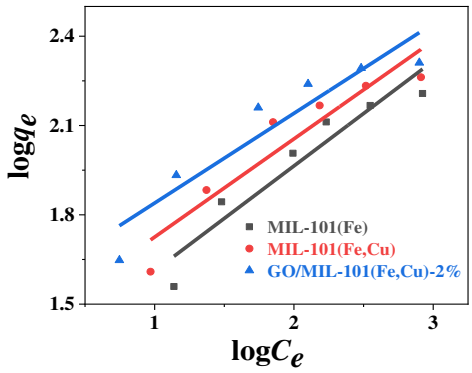

Figure 13. Fitting results of linearized Freundlich adsorption isotherms of phosphate adsorption on samples.

3.10 Adsorption thermodynamics

It can be seen from Figure 14 that MIL-101 (Fe), MIL-101(Fe,Cu) and GO/MIL-101(Fe,Cu)-2% had a certain effect on the removal of phosphate at different temperatures. With the increase of temperature, the adsorption capacity decreased gradually, which indicate that high temperature is not favorable in reaction process. High temperature might cause changes in the adsorbent and thus affected the adsorption performance.

By fitting the data in Figure 14, corresponding thermodynamic parameters can be obtained according to the following formula for adsorption thermodynamics.

$$\Delta G = \Delta H - T\Delta S \quad (7)$$

where ΔG is the change of Gibbs free energy, $J \cdot mol^{-1}$; ΔH is the change of adsorption enthalpy, $J \cdot mol^{-1}$; ΔS is the change of adsorption entropy, $J \cdot K^{-1} \cdot mol^{-1}$; T is the thermodynamic temperature, K.

$$\log K_d = \frac{\Delta S}{R} - \frac{\Delta H}{2.303RT} \quad (8)$$

where K_d is the distribution coefficient and R is the thermodynamic constant, which was 8.314 $J \cdot K^{-1} \cdot mol^{-1}$. The fitting results are shown in Figure 15 and the parameters are presented in Table 6. It can be seen from Table 6 that during the adsorption of phosphate of the three samples MIL-101 (Fe), MIL-101 (Fe,Cu) and GO/MIL-101 (Fe,Cu)-2%, ΔH values were all negative. The reaction of adsorption of phosphate is exothermic. ΔS was negative, indicating that the disorder at the solid-liquid interface decreased during the adsorption process, and when ΔG was negative, it was a spontaneous process. To sum up, the adsorption process of phosphate by the three samples was a spontaneous thermal reaction.

Table 6. Thermodynamic parameters of phosphate adsorption on samples.

Adsorbents	T/K	ΔG/(kJ·mol^{-1})	ΔH/(kJ·mol^{-1})	ΔS/(J·(K·mol)$^{-1}$)
MIL-101(Fe)	298.15	-7.46	-10.39	-9.84
	308.15	-7.36		
	318.15	-7.26		
	328.15	-7.16		
	338.15	-7.06		
MIL-101(Fe,Cu)	298.15	-11.82	-17.31	-18.40
	308.15	-11.64		
	318.15	-11.46		
	328.15	-11.27		
	338.15	-11.09		
GO/MIL-101(Fe,Cu)	298.15	-25.49	-38.84	-44.77
	308.15	-25.04		
	318.15	-24.60		
	328.15	-24.15		
	338.15	-23.70		

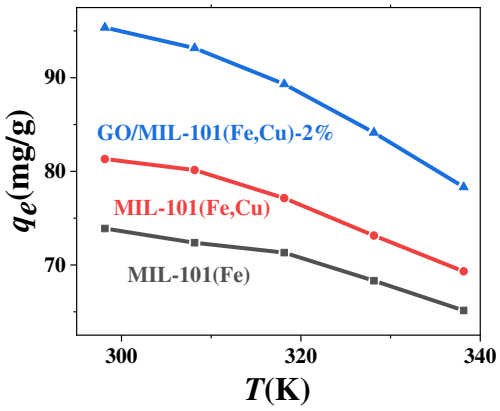

Figure 14. Effect of different temperatures.

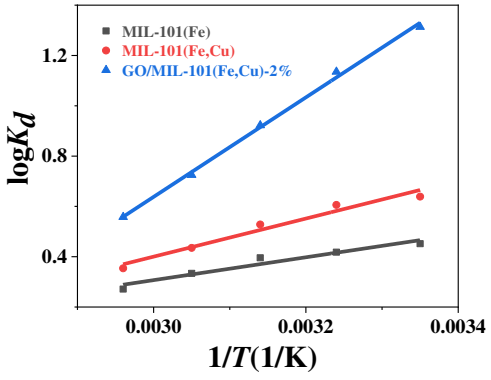

Figure 15. The logK_d~1/T relation diagram of phosphate adsorbed by samples.

3.11 Adsorption mechanism

3.11.1 Coordination bond

The formation of coordination bonds is an important mechanism for the adsorption of phosphoric acid on GO/MIL-101(Fe,Cu)-2%. Theoretically, there are unsaturated sites in the GO/MIL-101(Fe,Cu)-2% metal cluster, which can be used as Lewis acid sites to obtain M-OH through deprotonation in aqueous solution. From infrared spectrum analysis, similar results can be obtained. GO/MIL-101(Fe,Cu)-2% changed significantly before and after phosphate adsorption. As shown in Figure 4, after phosphate adsorption, a broad peak was formed at 1018.29 cm^{-1}, and a new peak appeared at 1106.69 cm^{-1}, corresponding to the P=O and P-O bonds, respectively. This result confirms that phosphate is adsorbed on GO/MIL-101(Fe,Cu)-2% by forming coordination bonds.

3.11.2 Electrostatic attraction

According to the influence of pH on the adsorption capacity, the effect of electrostatic attraction in the adsorption process can be clearly understood. Figure 7 display the effect of pH on the adsorption of phosphate by GO/MIL-101(Fe,Cu)-2%. During the adsorption process, the pH of the solution will affect the surface charge of GO/MIL-101(Fe,Cu)-2% and the ionization degree of pollutants. Phosphate has a low adsorption capacity under extremely acidic conditions(pH=2), after that the adsorption capacity increases rapidly (pH=3), and then the adsorption capacity decreases with increasing pH. The results of Zeta potential show that the IEP of GO/MIL-101(Fe,Cu)-2% is approximately between 7-8, which indicates that GO/MIL-101(Fe,Cu)-2% contains positive charges on the surface. Phosphate is anionic pollutants and under acidic conditions, when H^+ exists in a large amount, the adsorption effect is better. When the H^+ gradually decreases and the adsorption performance also decreases. Therefore, the electrostatic attraction in the adsorption process of phosphate plays an important role.

3.11.3 Hydrogen bond

It can be seen from the infrared results that some hydrogen bonds are formed between the oxygen in the phosphate structure and the hydroxyl groups of the composite material. These hydrogen bonds have a certain positive influence on the adsorption process and play a certain supplementary role for the adsorption capacity.

In summary, electrostatic attraction, forming coordination bonds and hydrogen bonds are the main mechanisms for the adsorption of phosphate by GO/MIL-101(Fe,Cu)-2%

3.12 Reusability

The experimental results of desorption regeneration are shown in Figure 16. As it can be seen from the figure, these three materials had a certain degree of reusability in the process of adsorbing phosphate. The reusability of the other MIL-101(Fe) and MIL-101(Fe,Cu) are obviously not as good as that of the composite material, and the adsorption performance decreases faster. It may be due to formation of strong coating structure in the composite material, which makes it more stable. After four times of adsorption-desorption the removal rate of phosphate by GO/MIL-101(Fe,Cu)-2% decreased from 96.11% to 72.13%, which proved that the material had good reusability.

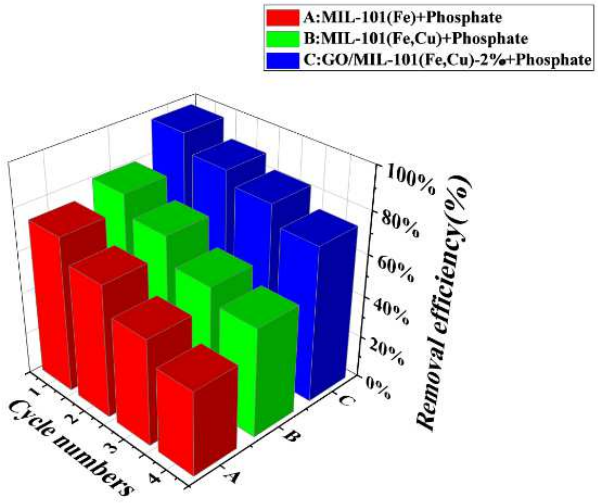

Figure 16. Regeneration cycles of MIL-101(Fe), MIL-101(Fe,Cu) and GO/MIL-101(Fe,Cu)-2% composite materials

4. Conclusion

The GO/MIL-101(Fe,Cu) composite adsorbent was prepared by hydrothermal reaction. Compared with MIL-101 (Fe), the specific surface area of MIL-101 (Fe,Cu) increased by 31.72%. The addition of GO provided a matrix for the synthesis of MIL-101 (Fe,Cu), result in enhancing of the pore structure, strong stability, exposing more active sites, enriching the adsorption mechanism. The ratio of the two (GO and MIL-101 (Fe,Cu)) plays a decisive role in the successful synthesis of the material. The experimental results shows that the adsorption capacity of GO/MIL-101(Fe,Cu)-2% is significantly better than that of MIL-101(Fe) and MIL-101(Fe,Cu).

According to the result of Langmuir and Freundlich adsorption isotherm data, the adsorption kinetic data are more in line with the second-order kinetic model and the Langmuir adsorption isotherm model, which indicate that the adsorption process is a single-molecular-layer adsorption. The main adsorption mechanism is electrostatic attraction, formation of coordination and hydrogen bonds. The fabricated material shown >70% phosphate removal rate after four cycles of adsorption-desorption, which proven that the GO/MIL-101(Fe,Cu)-2% surface is positively charged and has an ideal adsorption performance for anionic pollutants. To sum up, GO/MIL-101(Fe,Cu)-2% is a promising compatible adsorption material.

Author contributions You Wu designed the materials, conducted major adsorption experiments and wrote the manuscript of the paper. Zhuannian Liu provided guidance of the research, reviewed the manuscript and provided experimental resources. Bakhtari Mohammad Fahim conducted data processing and grammar review. Junnan Luo did the characterization experiment. All authors read and approved the final manuscript.

Funding This study was financially supported by the National Natural Science Foundation of China (51278418）

Availability of data and materials All authors agreed to state that required data and materials relevant will be available for further validity of the results presented.

Compliance with ethical standards

Ethical approval We assured that this manuscript is original work and this work neither accepted nor submitted simultaneously to any other journals.

Consent to participate All the authors listed have approved the manuscript.

Consent to publish This manuscript is approved by all authors for publication in Environmental Science and Pollution Research.

Competing interests The authors declare that they have no competing interests.

References

Adegoke KA, Bello OS (2015) Dye sequestration using agricultural wastes as adsorbents. Water Resources Indus 12:8-24. https://doi.org/10.1016/j.wri.2015.09.002.

Al-Alwani MAM, Ludin NA, Mohamad AB, Kadhum AAH, Mukhlus A (2018) Application of dyes extracted from Alternanthera dentata leaves and Musa acuminata bracts as natural sensitizers for dye-sensitized solar cells. Spectrochim Acta A 192:487-498. https://doi.org/10.1016/j.saa.2017.11.018.

Amini A, Khajeh M, Oveisi AR, Daliran S, Ghaffari-Moghaddam M, Delarami HS (2020) A porous multifunctional and magnetic layered

graphene oxide/3D mesoporous MOF nanocomposite for rapid adsorption of uranium(VI) from aqueous solutions. J Ind Eng Chem 93:322-332. https://doi.org/10.1016/j.jiec.2020.10.008.

Bacelo H, Pintor AMA, Santos SCR, Boaventura RAR, Botelho CMS (2020) Performance and prospects of different adsorbents for phosphorus uptake and recovery from water. Chem Eng J 381:122566. https://doi.org/10.1016/j.cej.2019.122566.

Barbosa ADS, Julião D, Fernandes DM, Peixoto AF, Freire C, de Castro B, Granadeiro CM, Balula SS, Cunha-Silva L (2017) Catalytic performance and electrochemical behaviour of Metal–organic frameworks: MIL-101(Fe) versus NH_2-MIL-101(Fe). Polyhedron 127:464-470. https://doi.org/10.1016/j.poly.2016.10.032.

Bu JQ, Yuan L, Ren YL, Liu YX, Meng Y, Peng X (2019) Enhanced removal of Eriochrome Black T in wastewater by Zirconium-based MOF/graphite oxide. Can J Chem 98. https://doi.org/10.1139/cjc-2019-0368.

Buhmann A, Papenbrock J (2013) Biofiltering of aquaculture effluents by halophytic plants: Basic principles, current uses and future perspectives. Environ Exp Bot 92:122-133. https://doi.org/10.1016/j.envexpbot.2012.07.005.

Burakov AE, Galunin EV, Burakova IV, Kucherova AE, Agarwal S, Tkachev AG, Gupta VK (2018) Adsorption of heavy metals on conventional and nanostructured materials for wastewater treatment purposes: A review. Ecotox Environ Safe 148:702-712. https://doi.org/10.1016/j.ecoenv.2017.11.034.

Chen H, Liu TL, Meng Y, Cheng Y, Lu J, Wang HS (2020) Novel graphene oxide/aminated lignin aerogels for enhanced adsorption of malachite green in wastewater. Colloid Surface A 603:125281. https://doi.org/10.1016/j.colsurfa.2020.125281.

Crini G (2006) Non-conventional low-cost adsorbents for dye removal: A review. Bioresource Technol 97:1061-1085. https://doi.org/10.1016/j.biortech.2005.05.001.

Deletic A, Wang HT (2019) Water Pollution Control for Sustainable Development. Engineering 5:839-840. https://doi.org/10.1016/j.eng.2019.07.013.

Dollimore D, Spooner P, Turner A (1976) The bet method of analysis of gas adsorption data and its relevance to the calculation of surface areas. Surf Technol 4:121-160. https://doi.org/10.1016/0376-4583(76)90024-8.

Dong Q, Shi SY, Xie YS, Wang YP, Zhang XQ, Wang XQ, Guo SY, Zhu LY, Zhang GH, Xu D (2020) Preparation of mesoporous zirconia ceramic fibers modified by dual surfactants and their phosphate adsorption characteristics. Ceram Int 46:14019-14029. https://doi.org/10.1016/j.ceramint.2020.02.201.

Drenkova-Tuhtan A, Schneider M, Franzreb M, Meyer C, Gellermann C, Sextl G, Mandel K, Steinmetz H (2017) Pilot-scale removal and recovery of dissolved phosphate from secondary wastewater effluents with reusable ZnFeZr adsorbent @ Fe_3O_4/SiO_2 particles with magnetic harvesting. Water Res 109:77-87. https://doi.org/10.1016/j.watres.2016.11.039.

Eltaweil AS, Elshishini HM, Ghatass ZF, Elsubruiti GM (2020) Ultra-high adsorption capacity and selective removal of Congo red over aminated graphene oxide modified Mn-doped UiO-66 MOF. Powder Technol 379:407-416 https://doi.org/10.1016/j.powtec.2020.10.084.

El-Yazeed WSA, El-Reash YGA, Elatwy LA, Ahmed AI (2020) Novel bimetallic Ag-Fe MOF for exceptional Cd and Cu removal and 3,4-dihydropyrimidinone synthesis. J Taiwan Inst Chem E 114:199-210. https://doi.org/10.1016/j.jtice.2020.09.028.

Emam HE, Abdelhameed RM, Ahmed HB (2020) Adsorptive Performance of MOFs and MOF Containing Composites for Clean Energy and Safe Environment. J Environ Chem Eng 8:104386. https://doi.org/10.1016/j.jece.2020.104386.

Fakhri H, Farzadkia M, Boukherroub R, Srivastava V, Sillanpää M (2020) Design and preparation of core-shell structured magnetic graphene oxide@MIL-101(Fe): Photocatalysis under shell to remove diazinon and atrazine pesticides. Sol Energy 208:990-1000. https://doi.org/10.1016/j.solener.2020.08.050.

Fu CC, Tran HN, Chen XH, Juang RS (2020) Preparation of polyaminated Fe_3O_4@chitosan core-shell magnetic nanoparticles for efficient adsorption of phosphate in aqueous solutions. J Ind Eng Chem 83:235-246. https://doi.org/10.1016/j.jiec.2019.11.033.

Gu Y, Xie DH, Wang YC, Qin WX, Zhang HM, Wang GZ, Zhang YX, Zhao HJ (2019) Facile fabrication of composition-tunable Fe/Mg bimetal-organic frameworks for exceptional arsenate removal. Chem Eng J 357:579-588. https://doi.org/10.1016/j.cej.2018.09.174.

Gupta NK, Saifuddin M, Kim S, Kim KS (2020) Microscopic, spectroscopic, and experimental approach towards understanding the phosphate adsorption onto Zn–Fe layered double hydroxide. J Mol Liq 297:111935. https://doi.org/10.1016/j.molliq.2019.111935.

He JJ, Xu YH, Wang W, Hu B, Wang ZJ, Yang X, Wang Y, Yang LW (2020) Ce(III) nanocomposites by partial thermal decomposition of Ce-MOF for effective phosphate adsorption in a wide pH range. Chem Eng J 379:122431. https://doi.org/10.1016/j.cej.2019.122431.

He L, Dong YN, Zheng YN, Jia QM, Shan SY, Zhang YQ (2019) A novel magnetic MIL-101(Fe)/TiO_2 composite for photo degradation of tetracycline under solar light. J Hazard Mater 361:85-94. https://doi.org/10.1016/j.jhazmat.2018.08.079.

Hou YB, Xu ZM, Yuan Y, Liu LX, Ma SC, Wang W, Hu Y, Hu WZ, Gui Z (2019) Nanosized bimetal-organic frameworks as robust coating for multi-functional flexible polyurethane foam: Rapid oil-absorption and excellent fire safety. Compos Sci Technol 177:66-72. https://doi.org/10.1016/j.compscitech.2019.04.018.

Huang WY, Zhang YM, Li D (2017) Adsorptive removal of phosphate from water using mesoporous materials: A review. J Environ Manage 193:470-482. https://doi.org/10.1016/j.jenvman.2017.02.030.

Isiuku BO, Enyoh CE (2020) Pollution and health risks assessment of nitrate and phosphate concentrations in water bodies in South Eastern, Nigeria. Environ Adv 2:100018. https://doi.org/10.1016/j.envadv.2020.100018.

Kyzas GZ, Deliyanni EA, Bikiaris DN, Athanasios CM (2018) Graphene composites as dye adsorbents: Review. Chem Eng Res Des 129:75-88. https://doi.org/10.1016/j.cherd.2017.11.006.

Lai KC, Lee LY, Hiew BYZ, Gopakumar ST, Gan SY (2018) Environmental application of three-dimensional graphene materials as adsorbents for dyes and heavy metals: Review on ice-templating method and adsorption mechanisms. J Environ Sci 79:174-199. https://doi.org/10.1016/j.jes.2018.11.023.

Langer M, Väänänen J, Boulestreau M, Miehe U, Bourdon C, Lesjean B (2017) Advanced phosphorus removal via coagulation, flocculation and microsieve filtration in tertiary treatment. Water Sci Technol 75:2875-2882. https://doi.org/10.2166/wst.2017.166.

Lebron YAR, Moreira VR, Drumond GP, Gomes GCF, da Silva MM, de Oliveira Bernardes R, Jacob RS, Viana MM, de Vasconcelos CKB, de Souza Santos LV (2020) Statistical physics modeling and optimization of norfloxacin adsorption onto graphene oxide. Colloid Surface A 606:125534. https://doi.org/10.1016/j.colsurfa.2020.125534.

Leo CP, Chai WK, Mohammad AW, Qi Y, Hoedley AF, Chai SP (2011) Phosphorus removal using nanofiltration membranes. Water Sci Technol 64:199-205. https://doi.org/10.2166/wst.2011.598.

Li YT, Ju WM, Yang L, Zhang LL, Sun YJ (2020) Adsorption behaviors and mechanism of graphene oxide for silver complex anion removal. Appl Surf Sci 529:147112. https://doi.org/10.1016/j.apsusc.2020.147112.

Li ZC, Liu XM, Jin W, Hu QS, Zhao YP (2019) Adsorption behavior of arsenicals on MIL-101(Fe): The role of arsenic chemical structures. J Colloid Interf Sci 554:692-704. https://doi.org/10.1016/j.jcis.2019.07.046.

Lin JL, Hu H, Gao NY, Ye JS, Chen YJ, Ou H (2020) Fabrication of GO@MIL-101(Fe) for enhanced visible-light photocatalysis degradation of organophosphorus contaminant. J Water Process Eng 33:101010. https://doi.org/10.1016/j.jwpe.2019.101010.

Liu RT, Chi LN, Wang XZ, Sui YM, Wang Y, Arandiyan H (2018) Review of metal (hydr)oxide and other adsorptive materials for phosphate removal from water. J Environ Chem Eng 6:5269-5286. https://doi.org/10.1016/j.jece.2018.08.008.

Liu YX, Li S, Wang C, Guo L, Wang YZ (2020) Accordion-like bimetal-organic framework anchoring on the partially-exfoliated graphite paper for high-performance supercapacitors. Appl Surf Sci 528:146954. https://doi.org/10.1016/j.apsusc.2020.146954.

Liu ZN, Fan AP, Han XG, Shapour H, Zhang QY (2020) PEI-modified chromium-based metal organic framework for Cr(VI) removal from aqueous solution. Desalin Water Treat 184:139-149. https://doi.org/10.5004/dwt.2020.24992.

Liu ZN, Fan AP, Ho CH (2020) Preparation of AC/Cu-BTC Composite and Its Adsorption Mechanisms. J Environ Eng 146:04020018. https://doi.org/10.1061/(ASCE)EE.1943-7870.0001678.

Loganathan P, Vigneswaran S, Kandasamy J, Bolan NS (2014) Removal and Recovery of Phosphate from Water Using Sorption. Crit Rev Env Sci Tec 44:847-907. https://doi.org/10.1080/10643389.2012.741311

Nebol'sin VA, Galstyan V, Silina YE (2020) Graphene oxide and its chemical nature: Multi-stage interactions between the oxygen and graphene. Surf Interfaces 21:100763. https://doi.org/10.1016/j.surfin.2020.100763.

Ogata F, Uematsu Y, Fukuda M, Saenjum C, Kabayama M, Nakamura T, Kawasaki N (2020) Changes in the mechanism of the reaction between phosphate and magnesium ions: Effect of initial concentration and contact time on removal of phosphate ions from aqueous media. J Environ Chem Eng 8:104385. https://doi.org/10.1016/j.jece.2020.104385.

Rego RM, Kuriya G, Kurkuri MD, Kigga M (2021) MOF based engineered materials in water remediation: Recent trends. J Hazard Mater 403:123605. https://doi.org/10.1016/j.jhazmat.2020.123605.

Santana CS, Olivares DMM, Silva VHC, Luzardo FHM, Velasco FG, de Jesus RM (2020) Assessment of water resources pollution associated with mining activity in a semi-arid region. J Environ Manage 273:111148. https://doi.org/10.1016/j.jenvman.2020.111148.

Sarma VVSS, Vivek R, Rao DN, Ghosh VRD (2020) Severe phosphate limitation on nitrogen fixation in the Bay of Bengal. Cont Shelf Res 205:104199. https://doi.org/10.1016/j.csr.2020.104199.

Srinivasan A, Viraraghavan T (2010) Decolorization of dye wastewaters by biosorbents: A review. J Environ Manage 91:1915-1929. https://doi.org/10.1016/j.jenvman.2010.05.003.

Strokal M, Kroeze C (2020) Water, society and pollution in an urbanizing world: recent developments and future challenges. Curr Opin Env Sust 46:11-15. https://doi.org/10.1016/j.cosust.2020.10.003.

Sun XB, Zhou YL, Zheng XG (2020) Comparison of adsorption behaviors of Fe-La oxides co-loaded MgO nanosheets for the removal of methyl orange and phosphate in single and binary systems. J Environ Chem Eng 8:104252. https://doi.org/10.1016/j.jece.2020.104252.

Tian YH, Yu ZC, Cao LY, Zhang XL, Sun CH, Wang DW (2021) Graphene oxide: An emerging electromaterial for energy storage and conversion. J Energy Chem 55:323-344. https://doi.org/10.1016/j.jechem.2020.07.006.

Wang L, Wang JY, He C, Lyu W, Zhang WL, Yan W, Yang L (2019) Development of rare earth element doped magnetic biochars with enhanced phosphate adsorption performance. Colloid Surface A 561:236-243. https://doi.org/10.1016/j.colsurfa.2018.10.082.

Wang Y.T., Wang KQ, Lin J, Xiao LQ, Wang XL (2020) The preparation of nano-MIL-101(Fe)@chitosan hybrid sponge and its rapid and efficient adsorption to anionic dyes. Int J Biol Macromol 165:684-2692. https://doi.org/10.1016/j.ijbiomac.2020.10.073.

Wang YF, Zhao W, Qi ZY, Zhang L, Zhang YN, Huang HO, Peng YZ (2020) Designing ZIF-8/hydroxylated MWCNT nanocomposites for phosphate adsorption from water: Capability and mechanism. Chem Eng J 394:124992. https://doi.org/10.1016/j.cej.2020.124992.

Zhang Y, Li HJ, Li MC, Li MH (2020) Adsorption of aniline on aminated chitosan/graphene oxide composite material. J Mol Struct 1209:127973. https://doi.org/10.1016/j.molstruc.2020.127973.

Zheng YQ, Cheng B, You W, Yu JG, Ho WK (2019) 3D hierarchical graphene oxide-NiFe LDH composite with enhanced adsorption affinity to Congo red, methyl orange and Cr(VI) ions. J Hazard Mater 369:214-225. https://doi.org/10.1016/j.jhazmat.2019.02.013.

Zhou X, Huang WY, Shi J, Zhao ZX, Xia QB, Li YW, Wang HH, Li Z (2014)A novel MOF/graphene oxide composite GrO@MIL-101 with high adsorption capacity of acetone. J Mater Chem A 2:4722-4730. https://doi.org/10.1039/C3TA15086K.

Figures

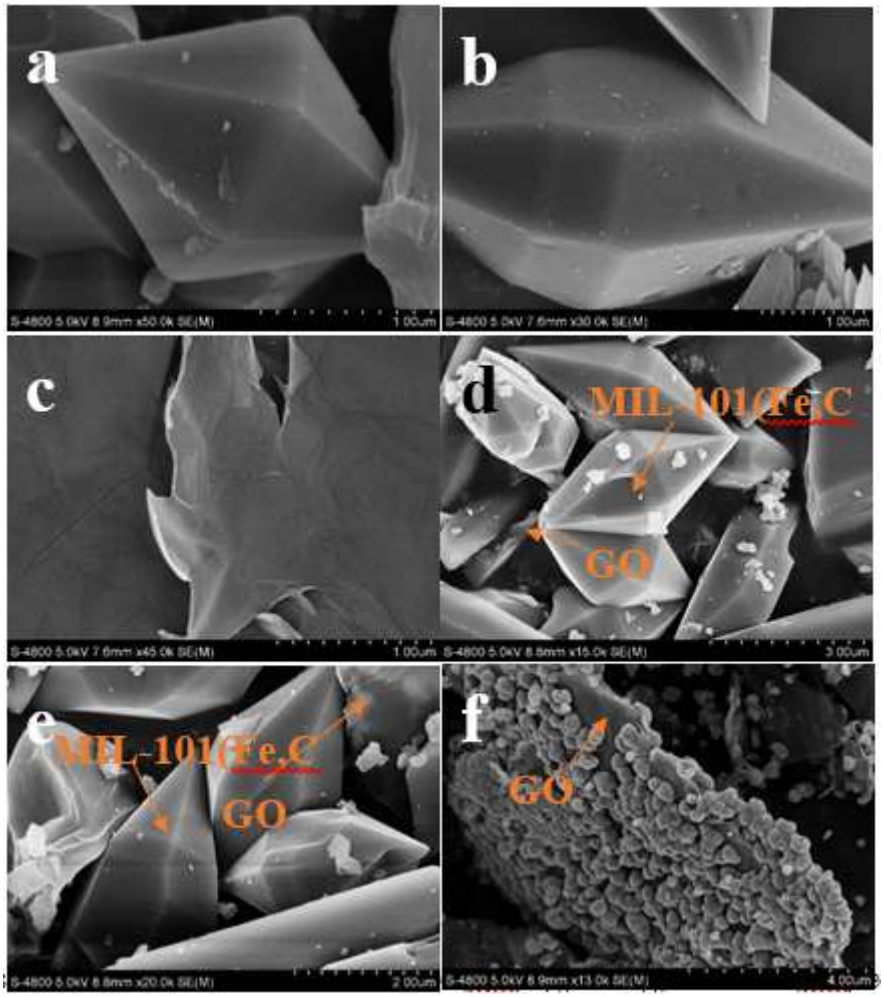

Figure 1

SEM images of the MIL-101(Fe) (a), MIL-101(Fe,Cu) (b), GO (c), GO/MIL-101(Fe,Cu)-2% (d-e) and GO/MIL-101(Fe,Cu)-10% (f).

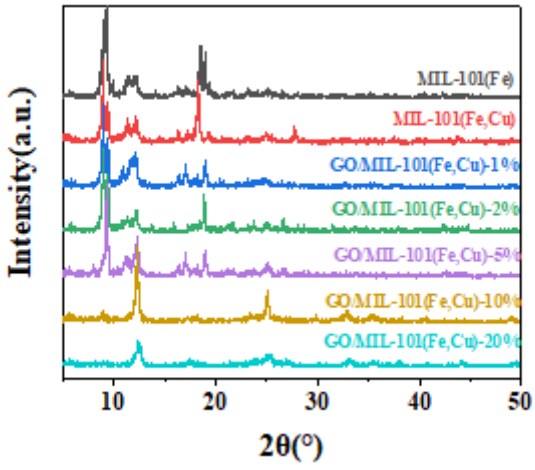

Figure 2

XRD patterns of samples.

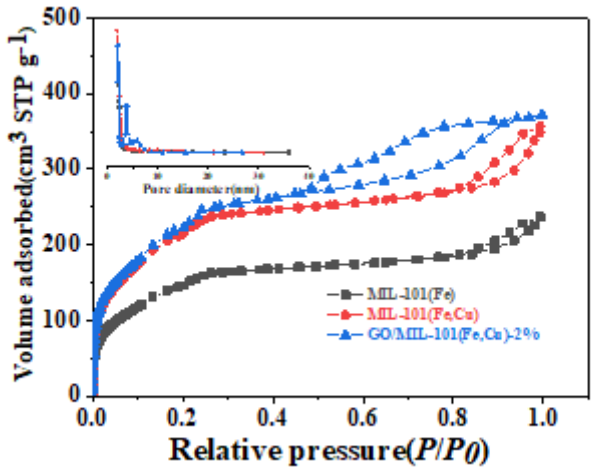

Figure 3

N2 adsorption–desorption isotherms and corresponding pore size distribution curves(inset) of samples.

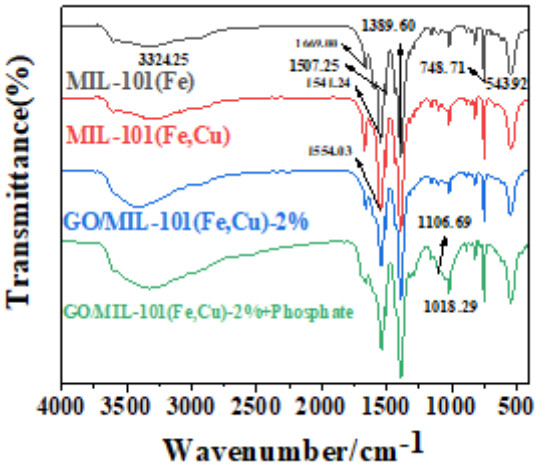

Figure 4

FTIR spectra of samples and GO/MIL-101(Fe,Cu)-2% after adsorption of phosphate.

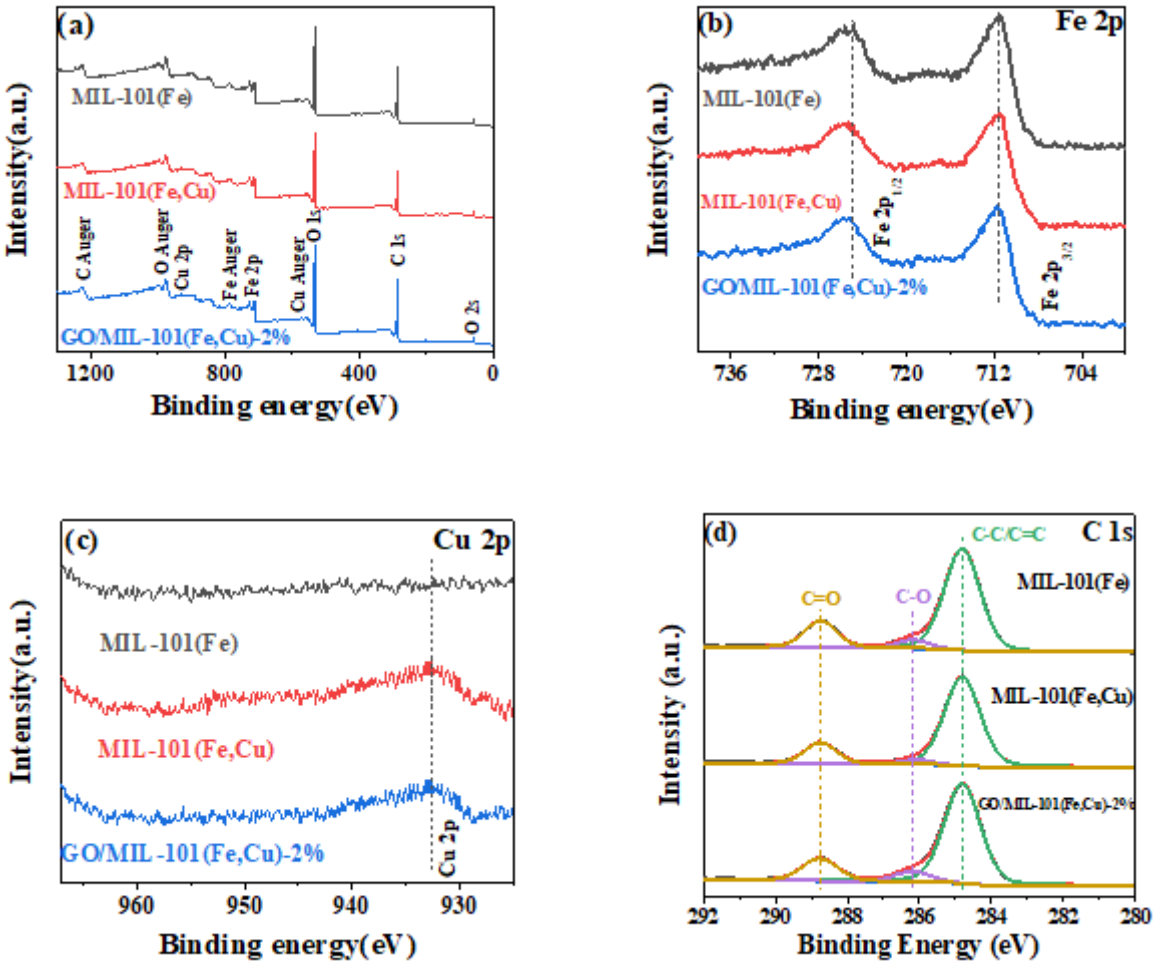

Figure 5

XPS survey spectra (a). High-resolution XPS of Fe 2p(b), Cu 2p(c), and C 1s regions(d) of samples.

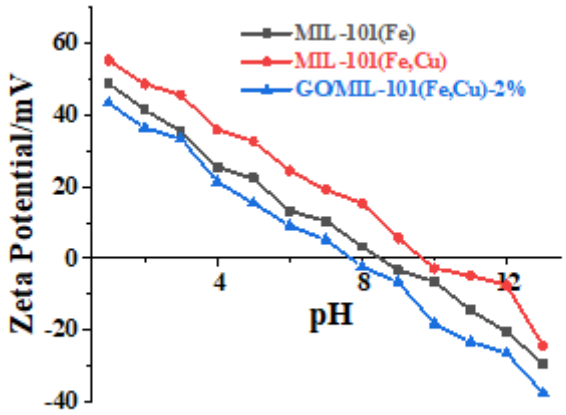

Figure 6

Distribution of zeta potentials of samples in aqueous solution.

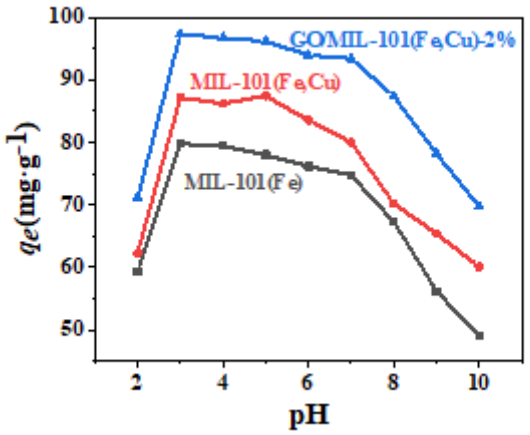

Figure 7

Effect of pH on adsorption of phosphate onto samples.

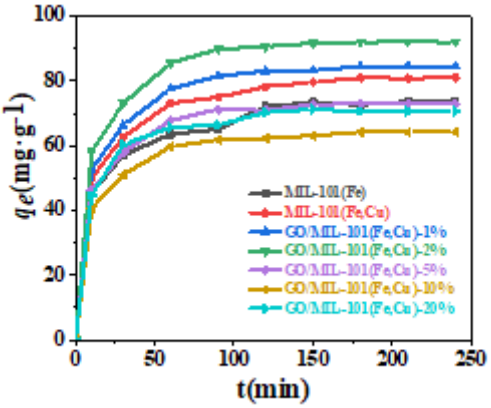

Figure 8

Adsorption of phosphate onto samples at different adsorption time.

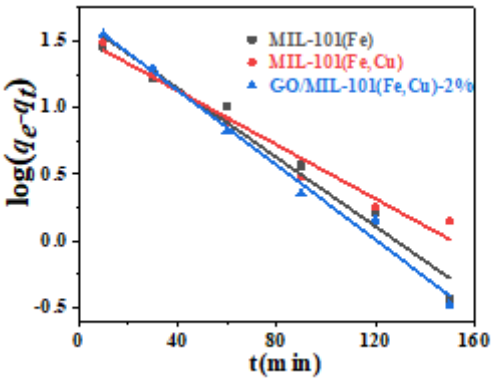

Figure 9

Lagergren first-order kinetics equation plot of phosphate.

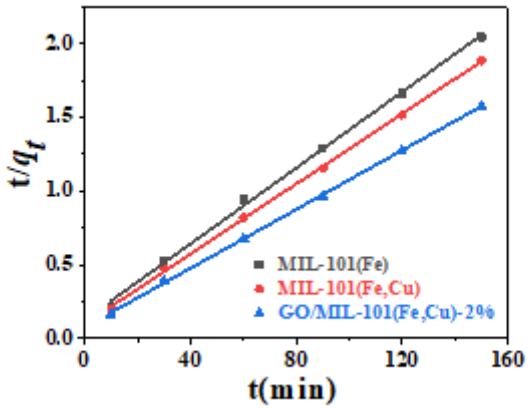

Figure 10

Lagergren second-order kinetics equation plot of phosphate.

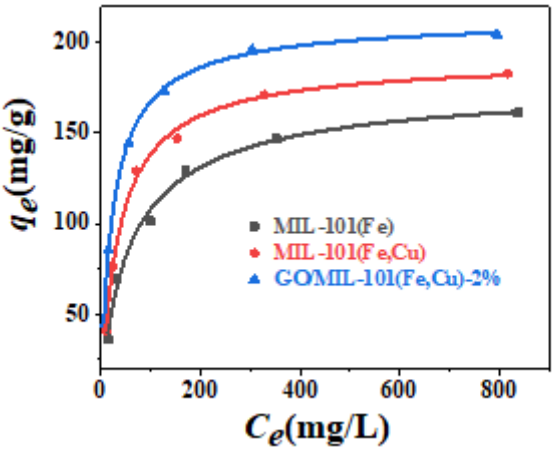

Figure 11

Phosphate adsorption isotherms for samples.

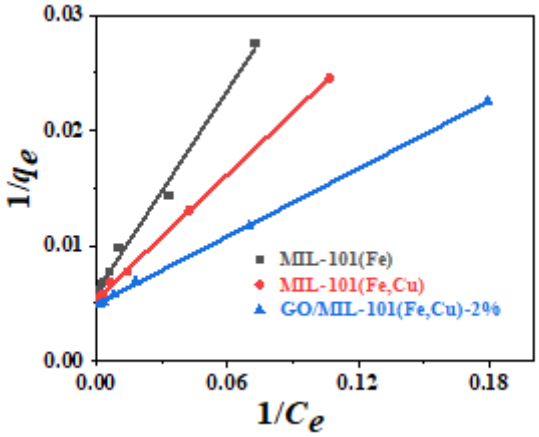

Figure 12

Fitting results of linearized Langmuir adsorption isotherms of phosphate adsorption on samples.

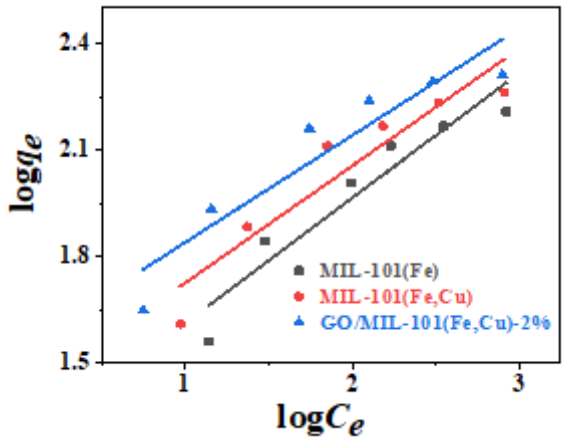

Figure 13

Fitting results of linearized Freundlich adsorption isotherms of phosphate adsorption on samples.

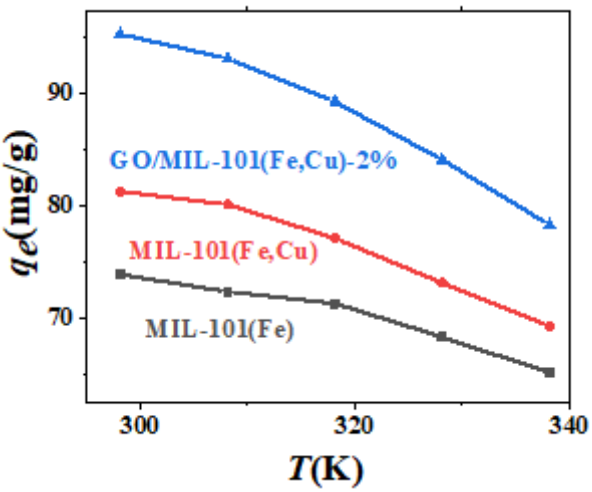

Figure 14

Effect of different temperatures.

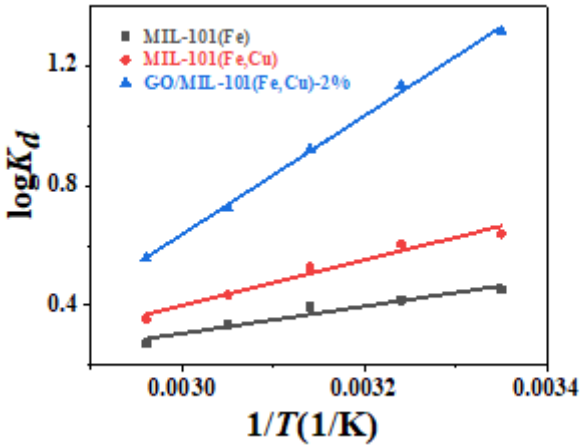

Figure 15

The logKd~1/T relation diagram of phosphate adsorbed by samples.

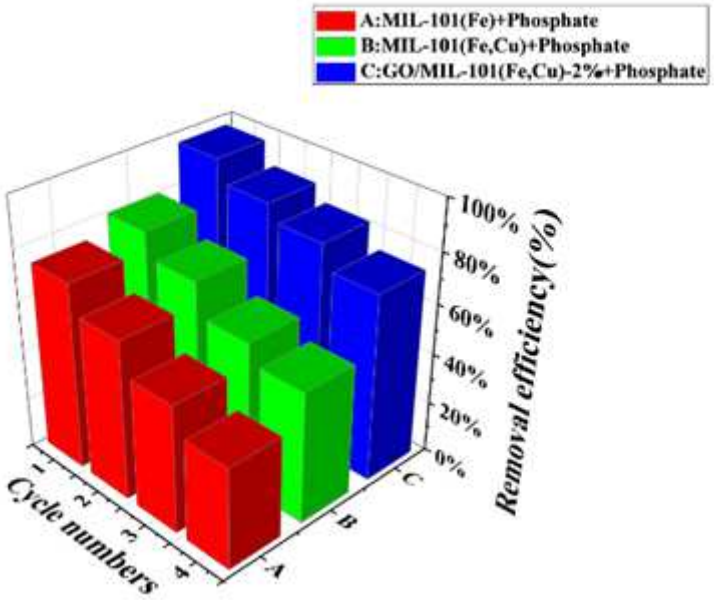

Figure 16

Regeneration cycles of MIL-101(Fe), MIL-101(Fe,Cu) and GO/MIL-101(Fe,Cu)-2% composite materials

Supplementary Files

This is a list of supplementary files associated with this preprint. Click to download.

- Graphicabstract.tiff